J. Iron Steel Res. Int.
https://doi.org/10.1007/s42243-024-01232-3

ORIGINAL PAPER

Effect of phase content on deformation compatibility in ferrite and bainite dual-phase steel: experimental and crystal plasticity finite element analysis

Xian-bo Shi[1,2] · Xing-yang Tu[3] · Bing-chuan Yan[4] · Yi Ren[1] · Wei Yan[2] · Yi-yin Shan[2]

Received: 8 January 2024 / Revised: 28 March 2024 / Accepted: 1 April 2024

Abstract
The phase volume fraction has an important role in the match of the strength and plasticity of dual phase steel. The different bainite contents (18–53 vol.%) in polygonal ferrite and bainite (PF + B) dual phase steel were obtained by controlling the relaxation finish temperature during the rolling process. The effect of bainite volume fraction on the tensile deformability was systematically investigated via experiments and crystal plasticity finite element model (CPFEM) simulation. The experimental results showed that the steel showed optimal strain hardenability and strength–plasticity matching when the bainite reached 35%. The 3D-CPFEM models with the same grain size and texture characters were established to clarify the influence of stress/strain distribution on PF + B dual phase steel with different bainite contents. The simulation results indicated that an appropriate increase in the bainite content (18%–35%) did not affect the interphase strain difference, but increased the stress distribution in both phases, as a result of enhancing the coordinated deformability of two phases and improving the strength–plasticity matching. When the bainite content increased to 53%, the stress/strain difference between the two phases was greatly increased, and plastic damage between the two phases was caused by the reduction of the coordinated deformability.

Keywords Polygonal ferrite and bainite dual phase steel · Phase content · Deformation compatibility · Crystal plasticity finite element simulation · Stress/strain difference

1 Introduction

With increasing difficulty of extracting large onshore oil fields and the continuous decline in oil production, marine oil has become an important field of oil development [1–4]. Marine oil pipelines are essential lifelines for offshore oil production systems since they are the primary means of transporting offshore oil resources. They must serve in harsh marine environments including low temperature and high-pressure condition. They not only must tolerate variations of static stresses including internal and external pressures, but also have to handle dynamic loads, such as the changes of the seabed, wind, waves, and S-shaped laying as well as J-shaped laying during pipeline installation [5, 6]. High-deformability pipeline steel with polygonal ferrite and bainite (PF + B) is the optimum dual phase microstructure to guarantee the safety of oil pipeline transportation [1]. Studies have indicated that the coexistence of soft and hard phases improved strain-hardening behavior, which improved its strength and ensured its deformability [7]. The key factors affecting the strength and plasticity of dual phase steel included phase volume fraction, grain size, and phase distribution morphology [8–12]. However, there was a significant contradiction in the influence of phase content on strength–plasticity. Akbarpour and Ekrami [13] investigated the effect of bainite content on the strength and plasticity of PF + B

Xian-bo Shi and Xing-yang Tu have contributed equally to this work.

✉ Xing-yang Tu
txy2130@163.com

[1] State Key Laboratory of Metal Material for Marine Equipment and Application, Anshan 114009, Liaoning, China

[2] Institute of Metal Research, Chinese Academy of Sciences, Shenyang 110016, Liaoning, China

[3] Northwest Nonferrous Metal Research Institute, Xi'an 710000, Shaanxi, China

[4] PipeChina North Pipeline Company, Langfang 006500, Hebei, China

Published online: 21 June 2024

dual phase steel. Results showed that the yield strength and tensile strength of the experimental steel gradually increased and plasticity gradually decreased with the bainite increasing. The work of Zhang et al. [14] showed that the yield strength and tensile strength of PF + B dual phase steel exhibited a two-stage variation rule with the bainite increasing. When the bainite content was less than 40%, the strength decreased with the increase in bainite volume fraction. When bainite was the matrix, the strength increased with the increase in bainite volume fraction. Whether bainite or ferrite as the matrix, its plasticity gradually decreased with the increase in bainite. Tang et al. [15] reported that as the volume fraction of bainite increased, the strain hardening exponent and uniform elongation of PF + B dual phase steel first increased and then decreased, and the yield strength ratio showed the opposite trend, reaching the maximum value when the bainite volume fraction was about 30%. The contradictory research results should be reduced by the inability to control other variables (like grain size and texture) during the research process.

The finite element simulation method based on the actual microstructure characteristics of microstructure can be used to analyze the influence of a single variable on strength and plasticity. Ishikawa et al. [16] studied the plastic deformation behavior of PF + B dual phase steel with bainite volume fraction of 16% and 46%, respectively. The digital image correlation (DIC) method and representative volume element (RVE) method were used to characterize and simulate the stress/strain during the deformation process. However, their results ignored the influence of crystallographic parameters of each phase. Liu et al. [17] established a crystal plasticity finite element model (CPFEM) based on the measured crystallographic parameters and grain size distribution characteristics of ferrite and martensite (F/M) dual phase steel, and the influence of a single texture feature on strength-plasticity in F/M dual phase steel was analyzed. The results indicated that the initial crystal orientation significantly influenced the localization of shear strain and damage behavior.

In this work, PF + B dual phase steel with different bainite contents (18–53 vol.%) was obtained by the thermal–mechanical controlling process. The 3D-CPFEM were established according to the actual microstructure characterization to analyze the effect of single bainite variable on the microstructural stress–strain distribution and strength-plasticity during deformation.

2 Experimental

2.1 Materials

The experimental steel used in this study was smelted in a vacuum induction melting furnace and cast into ingots. Subsequently, a billet with the size of 300 mm × 100 mm × 260 mm was obtained through free forging. The chemical composition of the experimental steel is shown in Table 1. A_{r1} and A_{r3} temperatures were determined as 660 and 740 °C, respectively.

The experimental steels with different phase contents were obtained through a hot rolling process. The original thickness of the steel billet was 80 mm. The billet was reheated to 1200 °C for 2 h, and then was rolled to the thickness of 32 mm through 8 passes. Controlling the relaxation termination temperature obtained PF + B dual phase steel with different bainite volume fractions. Setting the relaxation termination temperature (RTT) after rolling at the dual phase zone (between A_{r1} and A_{r3}), the specific temperatures were 720, 700, 680, and 660 °C, respectively. Subsequently, the billets were cooled to 360 °C at a cooling rate of ∼ 15 °C /s, and finally air cooled to room temperature. The specific rolling process route is shown in Fig. 1.

2.2 Microstructural characterization and mechanical property test

The specimens were obtained from the rolling billet by cut machine, and then subjected to grinding, polishing and etching (4 vol.% Nital solution for about 15 s). Microstructure was observed along the rolling direction (RD)–normal direction (ND) plane by optical microscopy (OM) and scanning electron microscopy (SEM). 10 OM images were selected for calculating the volume fraction of the bainite through ImageJ software. The electron backscatter diffraction (EBSD) analysis tests were conducted by Zeiss Gemini SEM 300 field emission scanning microscopy (FE-SEM). The specimens were electropolished at − 20 °C in an electrolyte solution containing 10 vol.% perchloric acid and 90 vol.% alcohol with a Tenu-Pol-5 electrolytic polishing machine, and the voltage and scanning step used for EBSD data collection were 20 kV and 0.15 μm, respectively.

The dog-bone-shaped tensile specimens with gauge length of 20 mm and diameter of 3 mm were prepared along the rolling direction. The room temperature tensile tests were conducted on the SANS-CMT 5205 tensile machine at a strain rate of 1.0×10^{-3} s^{-1}. The tensile fracture morphologies were observed by SEM.

Nanoindentation experiments were conducted on bainite and polygonal ferrite phases to study the micromechanical properties. The load–displacement curve to describe the changes in the material during compression under external forces, and the loading–unloading curve was used to analyze the experimental results. Firstly, the nanoindentation test specimens was electropolished and positioned using a Vickers hardness tester. Subsequently, nanoindentation

Table 1 Chemical compositions of experimental steel (wt.%)

C	Si	Mn	P	S	Al	N	Cr	Cu	Ni	Nb	V	Ti	Mo	Fe
0.06	0.22	1.6	0.012	0.002	0.03	0.007	0.11	0.01	0.01	0.05	0.006	0.02	0.05	Balance

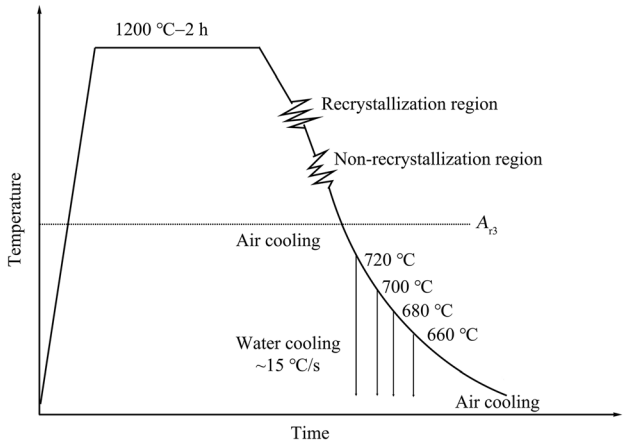

Fig. 1 TMCP process for preparation of PF + B dual phase steel with different phase contents

experiments were conducted on the polygonal ferrite and bainite corresponding to the positioning area. The test was conducted on the Triboundeter nanoindentation mechanical tester, using a Berkovich triangular conical indenter with a curvature radius of approximately 100 nm. The maximum loading force during the experiment was 4000 μN, with loading time of 5 s and a constant loading rate of 0.5 mN/s.

2.3 Crystal plasticity model

The crystal plasticity (CP) method based on single crystals has been successfully applied to predict the mechanical response of polycrystalline materials. The deformation amount F in single crystal deformation can be expressed as Eq. (1) [18]:

$$F = \frac{\partial x}{\partial X} \tag{1}$$

where X and x represent the initial and current positions of particles in a single crystal, respectively. F can be decomposed into plastic shear deformation (F_p) and elastic deformation (F_e). F_p is mainly related to crystal rotation, slip, and twinning, while F_e is mainly caused by lattice stretching and lattice distortion, and it is assumed that F_e is not affected by crystal slip. However, F_p cannot be represented by simple parameters, but rather by plastic deformation rate gradients [19]:

$$\dot{F}_p = LF_p \tag{2}$$

where L is the rate gradient [20], and it is related to the slip systems and twinning initiated during internal deformation of grains, which can be expressed as:

$$L = \sum_{\alpha=1}^{N} \dot{\gamma}^{(\alpha)} m^{(\alpha)} \otimes n^{(\alpha)} \tag{3}$$

where α represents slip systems; $\dot{\gamma}^{(\alpha)}$ represents the shear rate of α slip systems; $m^{(\alpha)}$ and $n^{(\alpha)}$ represent the united vectors of slip direction and the normal direction of slip plane; and N is the number of the activated slip systems. $\dot{\gamma}^{(\alpha)}$ is mainly determined by the initial shear rate ($\dot{\gamma}_0$), and the relationship of the shear stress on this slip system ($\tau_0^{(\alpha)}$) and the critical shear stress of the slip system to initiate movement ($\tau_c^{(\alpha)}$) can be determined as:

$$\dot{\gamma}^{(\alpha)} = \dot{\gamma}\left(\frac{\tau_0^{(\alpha)}}{\tau_c^{(\alpha)}}\right)^{\frac{1}{m}} \operatorname{sign}\left(\tau_0^{(\alpha)}\right) \tag{4}$$

where m is the strain rate sensitivity index and is determined as 0.5 for this material. $\dot{\gamma}_0$ is related to the type of phase in the microstructure. In each slip system, $\tau_c^{(\alpha)}$ is defined by the Piola–Kirchhoff stress, and it can be calculated using Eq. (5):

$$\dot{\tau}_c^{(\alpha)} = \sum_{\beta}^{N} h_{\alpha\beta}\dot{\gamma}^{(\beta)} \tag{5}$$

where β represents slip systems; $h_{\alpha\beta}$ is the strain hardening rate; and $\dot{\gamma}^{(\beta)}$ is the shear rate of β slip systems. Accumulated shear strain of all slip systems (γ) can be expressed as:

$$\gamma = \sum_{\alpha=1}^{N} \int_0^t \left|\dot{\gamma}^{(\alpha)}\right| \mathrm{d}t \tag{6}$$

where t is the loading time. During the plastic deformation process of polycrystals, there is deformation heterogeneity within and among grains. The orientation inside the grains will gradually change with the deformation process, and coordinated deformation was formed among grains through the interaction between slip and grain boundaries. This led to the transformation of the grain orientation that was originally easy to deform into an orientation not conducive to deformation, and the unfavorable orientation became a

favorable orientation. In addition, while dislocations were formed inside the grains, the sharpening of the dislocation envelope will gradually increase the orientation difference at the sub-grain boundaries. As the density of dislocations increased, entanglement occurred among dislocations, leading to an increase in material strength and a decrease in plasticity, and resulting in strain hardening of the material. This caused the critical shear stress initiated by the slip system in the crystal to increase with the increase in strain, and the plastic deformation process of the material was closely related to its strain hardening rate. $h_{\alpha\beta}$ of the material can be expressed by the following equation:

$$h_{\alpha\beta} = q_{\alpha\beta}\left[h_0\left(1-\frac{\tau_0^{(\beta)}}{\tau_c^{(\beta)}}\right)^a\right] \tag{7}$$

Thus, the critical shear stress of the slip system can be expressed as:

$$\tau_c^{(\alpha)} = \tau_0^{(\alpha)} + \int_0^t q_{\alpha\beta}\left[h_0\left(1-\frac{\tau_0^{(\beta)}}{\tau_c^{(\beta)}}\right)^\alpha\right]\dot{\gamma}^{(\beta)}\mathrm{d}t \tag{8}$$

where $\tau_0^{(\beta)}$ and $\tau_c^{(\beta)}$ refer to the shear stress of the β slip system and the critical shear stress of the slip system initiation, MPa, respectively; h_0 and a are the initial hardening modulus parameter between among slip systems; and $q_{\alpha\beta}$ is the hardening coefficient among different slip systems, which is self-hardening in this model and always has a value of 1. In the present study, the slip systems considered in the simulation were mainly {110}<111> and {112}<111> , with a total of 24 slip systems. In summary, the material parameters that need to be determined during simulation are summarized in Table 2.

Table 2 Material parameters in phenomenological power-law model

Description	Mechanical parameter
Elastic constant/MPa	C11
Elastic constant/MPa	C12
Elastic constant/MPa	C44
Reference shear strain rate	$\dot{r}$
Critical resolved shear stress/MPa	τ_c
Initial shear stress/MPa	τ_0
Initial hardening rate	h_0
Hardening exponent	a
Strain rate exponent	m

3 Results and discussion

3.1 Microstructures

The microstructures with different RTTs are presented in Fig. 2. The volume fraction of bainite decreased as RTT decreased. The long relaxation time contributed to enhancing the driving force of austenite to ferrite transformation. Thus, ferrite experienced a long nucleation and growth time, leading to a decrease of bainite.

The volume fraction of bainite was obtained by counting 10 metallographic microstructure images. The evolution law of bainite content with RTT is presented in Fig. 3a, and the variety rule of bainite content was consistent with the results observed in Fig. 2. The bainite content was determined as 18% (660 °C), 27% (680 °C), 35% (700 °C), and 53% (720 °C) in different RTTs, respectively. In order to minimize the effect of grain size, areas on each hot-rolled steel plate with small difference in average grain size were selected for subsequent research. The grain size distribution at the selected location is shown in Fig. 3b. The results indicated that the average grain size of polygonal ferrite in the selected area was within 5–7 μm. For convenience, the specimens with different bainite contents were named as PF + 18%B, PF + 27%B, PF + 35%B, and PF + 53%B, respectively.

3.2 Mechanical properties

Figure 4a shows the engineering stress–strain curves of four specimens. There are no obvious yield plateau and it presents a continuous yield characteristic. The variation rule of yield strength, tensile strength, total elongation, and uniform elongation of each specimen are shown in Fig. 4b. The specific mechanical properties are shown in Table 3. As the volume fraction of bainite increased, the yield strength gradually increased, but when the bainite content was below 35%, the tensile strength did not change much. The total elongation and uniform elongation showed a trend of increasing first and then decreasing with the increase in bainite content, reaching the maximum value when the bainite was 35%. The strain hardenability of steel was usually represented by the strain hardening index (n). The higher the value of n, the higher the strain hardenability of the steel. The strain hardening index can be fitted to $\ln\sigma$–$\ln\varepsilon$ of the uniform plastic deformation stage based on the Hollomon equation (Eq. (9)). The curve was obtained as shown in Eq. (10) [21]:

$$\sigma = K\varepsilon^n \tag{9}$$

$$\ln\sigma = \ln K + n\ln\varepsilon \tag{10}$$

where σ is true stress, MPa; ε is true strain; and K is the strength coefficient, MPa.

As shown in Fig. 4b, the variation rule of the strain hardening index was consistent with that of elongation. When the bainite content was 35%, the strain hardening

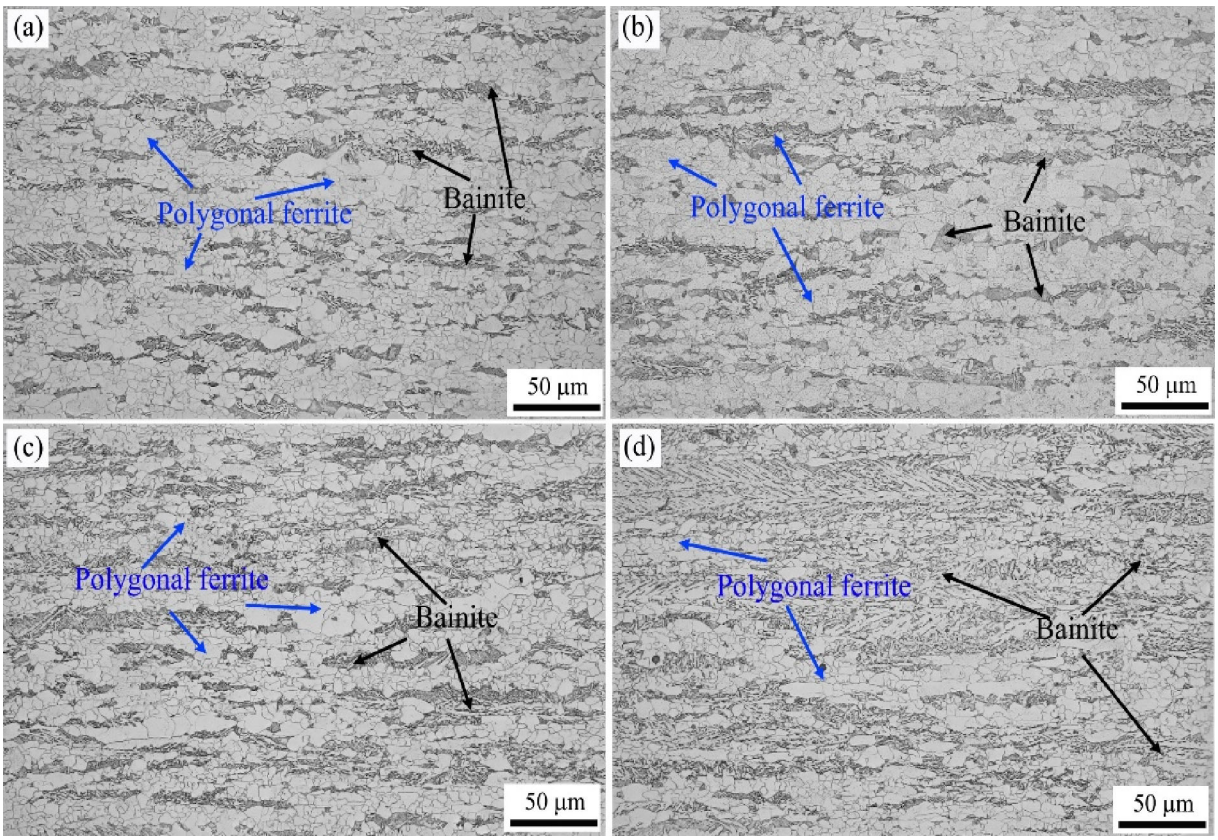

Fig. 2 Microstructure of PF + B dual-phase steel with different relaxation termination temperatures. **a** 660 °C; **b** 680 °C; **c** 700 °C; **d** 720 °C

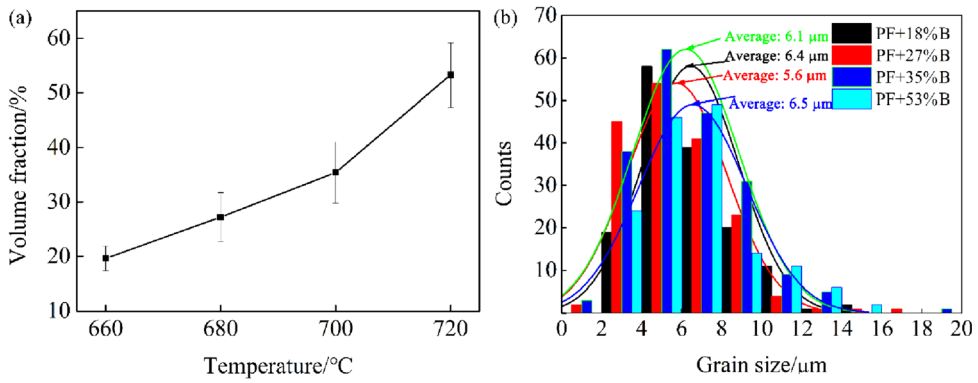

Fig. 3 Evolution rule of bainite volume fraction (**a**) and grain size (**b**) of PF after different relaxation termination temperatures

index also reached its maximum value, indicating that the strain hardenability of the steel was optimal at this time. According to the variation law of comprehensive mechanical properties, the steel has the optimal strength–plasticity matching when the bainite reached 35%.

In ferrite + martensite dual-phase steel, the elongation usually showed a gradual decrease as the martensite increased [22]. High martensite content could induce martensite to bear greater strain during deformation, thereby increasing the rate of micro-void initiation and making it more prone to unstable propagation, and finally resulting in fracture. In general, the strain will preferentially transfer to the bainite as the bainite increases in PF + B dual phase steel, leading to a decrease in its plasticity. However, in this study, the elongation did not show a monotonic decrease trend, but reached its peak at a bainite volume fraction of 35%. This result was similar to the research results of Tang et al. [15]. Nonetheless, the existing studies have not focused on the influence of volume fraction on the microstructure deformation characteristics and plastic damage behavior during the deformation process. In order to clarify the reason for

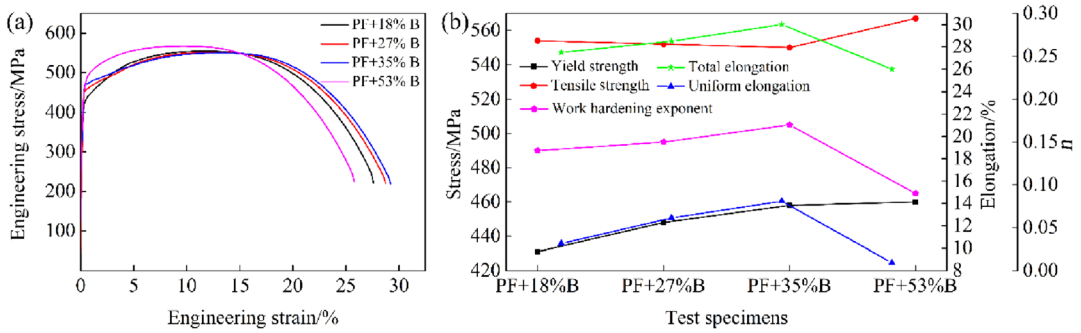

Fig. 4 Engineering stress–strain curves (**a**) and tensile properties (**b**) of experimental steels

Table 3 Mechanical properties of four specimens

Specimen	R_m/MPa	R_{eL}/MPa	R_{eL}/R_m	n	A/%	UEL/%
PF + 18%B	554	431	0.77	0.14	27.5	10.4
PF + 27%B	552	448	0.81	0.15	28.5	12.7
PF + 35%B	550	458	0.83	0.17	30.0	14.2
PF + 53%B	567	460	0.81	0.09	26.0	8.7

R_m—Tensile strength; R_{eL}—yield strength; A—total elongation; UEL—uniform elongation

achieving the optimal strength plastic matching when the bainite content was 35%, the present study investigated the plastic deformation damage mechanism of PF + B dual phase steel by 3D-CPFEM analysis.

3.3 Establishment of 3D-CPFEM

Based on EBSD data, a 3D-CPFEM was established. The grain in bainite with high angle grain boundary (> 15°) was defined as an effective grain that affected deformation behavior [23, 24]. The grain size distribution of polygonal ferrite and bainite is shown in Fig. 5a. The 3D-CPFE models with bainite volume fractions of 18%, 35%, and 53% were constructed using DREAM 3D software [25], as shown in Fig. 5b and c, with a model size of 100 μm × 100 μm × 5 μm. Figure 5b presents the phase distribution map, and Fig. 5c shows the crystal orientation distribution (COD) map. The orientation distribution map (Fig. 5e) of bainite and polygonal ferrite in the model was established, which had similar characteristics to the pole map (Fig. 5d) measured in PF + 18%B specimen. During simulation, the material was loaded along x direction at a loading rate of 1×10^{-3} s^{-1}, with loading time of 250 s.

3.4 Determination of material parameters

To determine the mechanical properties of polygonal ferrite and bainite phase in multiphase materials, the nanoindentation method was used. The stress–strain curve of the corresponding phase can be obtained through reverse inference. In the present study, the combination of 3D-CPFE and nanoindentation inverse method was used to obtain the material constitutive parameters required for the crystal plasticity finite element simulation of the studied PF + B dual phase steel. The entire process is shown in Fig. 6.

The plastic behavior of many pure and alloy metals can be approximated by the power law, and the true stress–strain relationship can be represented by Eq. (11) [26]:

$$\sigma = \begin{cases} E\varepsilon & \sigma \le \sigma_y \\ \sigma_y(1 + E\varepsilon_p/\sigma_y)^n & \sigma > \sigma_y \end{cases} \quad (11)$$

where ε_p is the strain during the plastic deformation stage; σ_y is the yield strength, MPa; and E is elastic modulus, GPa.

The load–displacement curves of PF and bainite are shown in Fig. 7a. Figure 7b shows the typical indentation response curve (P–h curve), where P is the load, and h is displacement parameter, in which the relevant parameters that determine mechanical properties and stress/strain characteristics are described. The load–displacement curve is considered to follow Kick's power law, $P = Ch^2$, where C depends on the elastic–plastic material properties and the geometry of the indenter [27]. At the maximum depth h_m or maximum load P_m, the average contact pressure $P_{ave} = P_m/A$ (A is the true contact area measured at h_m) can be considered as the hardness (H) of the indentation material. After unloading, the slope of P–h was initially linear,

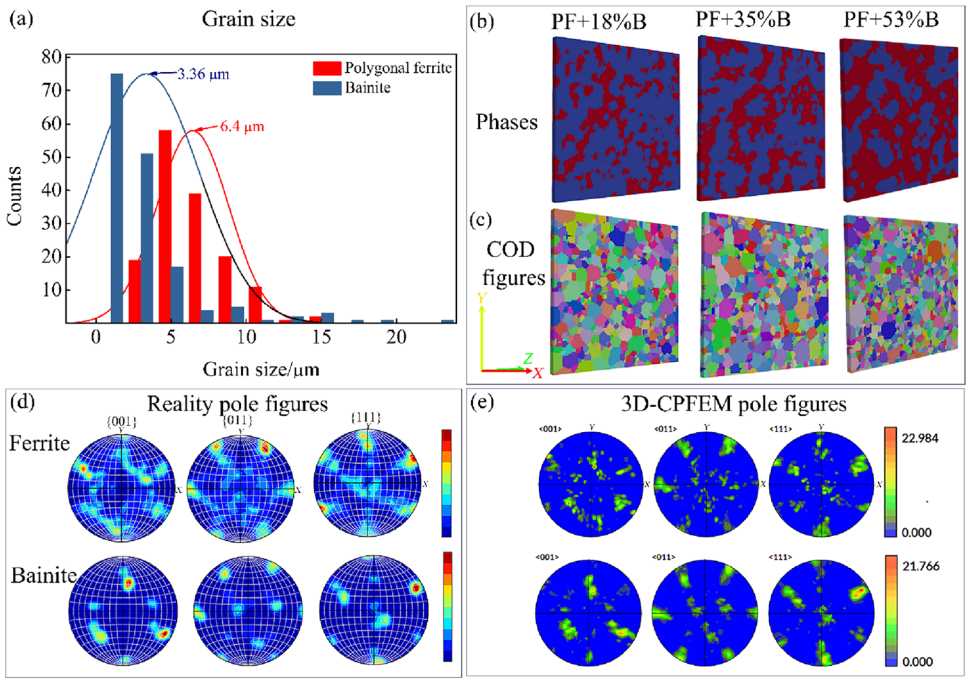

Fig. 5 Parameters for CPFE model and corresponding 3D-CPFE model. **a** Effective grain size distribution; **b** phase distribution map; **c** crystal orientation distribution; **d** reality pole figures of PF and bainite; **e** pole figures of established models

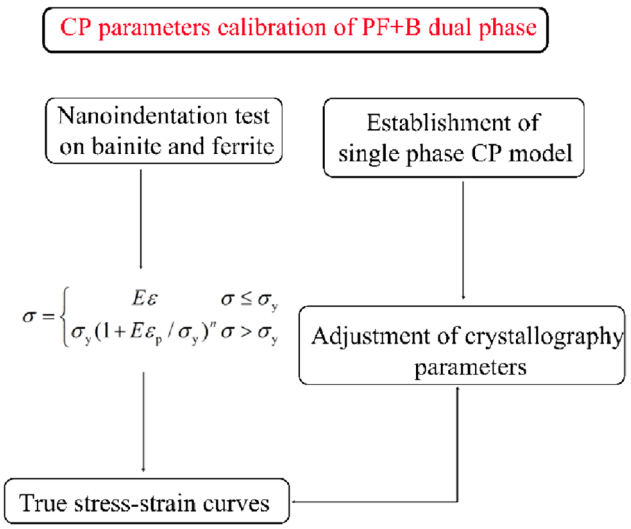

Fig. 6 Material parameters calibration process

where P_u was the unloading force. When fully unloaded (zero load), the remaining depth was h_r. The area below the loading and unloading curves represented the total work of loading W_t and elastic unloading W_e, respectively. Therefore, the area enclosed by the loading and unloading curves was the plastic work (W_p) during the indentation process, $W_p = W_t - W_e$.

During the nanoindentation experiment, n value of a material was easily obtained from the relationship between W_p and W_t (or h_r, h_m), and the degree of elastic rebound will depend on the degree of hardening. The yield strength of materials was generally obtained by analyzing the curvature C during the loading process. The research [28] indicated that $\sigma_{0.033}$ was independent of strain hardening, where E_r is contact modulus, and $\sigma_{0.033}$ can be presented in Eq. (12):

$$\frac{C}{\sigma_{0.033}} = -1.131\left[\ln\left(\frac{E_r}{\sigma_{0.033}}\right)\right]^3 + 13.635\left[\ln\left(\frac{E_r}{\sigma_{0.033}}\right)\right]^2 - 30.594\left[\ln\left(\frac{E_r}{\sigma_{0.033}}\right)\right] + 29.267 \tag{12}$$

The strain hardening index can be obtained from Eq. (13):

$$\frac{1dP_u}{E_r h_m dh}|h_m = (-1.40557n^3 + 0.77526n^2 + 0.15830n - 0.06831)\left[\ln\left(\frac{E_r}{\sigma_{0.033}}\right)\right]^3 + (17.93006n^3 - 9.22091n^2 - 2.37733n + 0.86295)\left[\ln\left(\frac{E_r}{\sigma_{0.033}}\right)\right]^2 + (-79.99715n^3 + 40.55620n^2 + 9.00157n - 2.54543)\left[\ln\left(\frac{E_r}{\sigma_{0.033}}\right)\right] + (122.65069n^3 - 63.88418n^2 - 9.5893n + 6.20045) \tag{13}$$

The calculated strength and strain hardening index of bainite and PF are shown in Table 4.

The calculated true stress–strain curves of bainite and polygonal ferrite are shown in Fig. 7c, and CPFEM of bainite and polygonal ferrite used for simulation is shown in Fig. 7d. By adjusting the constitutive parameters, it can

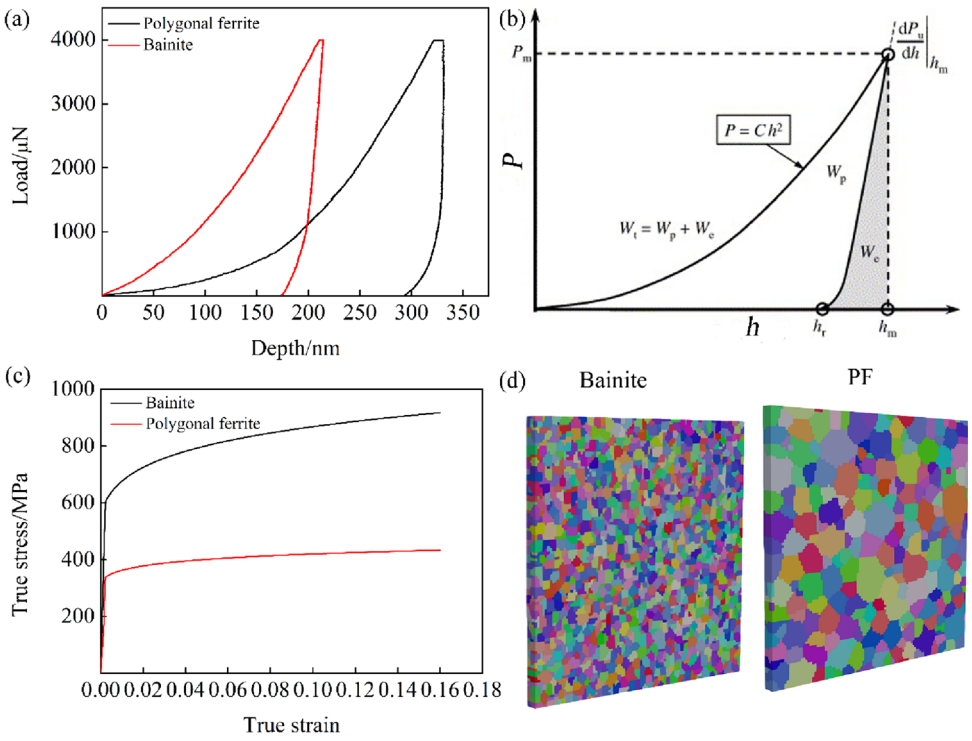

Fig. 7 Mechanical properties and model of bainite and polygonal ferrite single-phase. **a** Load–displacement curves; **b** typical nanoindentation curve; **c** reverse calculation of true stress–strain curve; **d** CPFE model

Table 4 Key parameters for reverse analysis of true strain–stress curves of PF and bainite

Phase	E_r/GPa	σ_y/MPa	H/GPa	n
Polygonal ferrite	135.344	323	1.354	0.07
Bainite	202.722	564	3.024	0.12

Table 5 Material parameters in phenomenological power-law model for bainite and ferrite

Mechanical parameter	Bainite	Polygonal ferrite
C11	282×10^3	233.3×10^3
C12	121×10^3	135.5×10^3
C44	100×10^3	118.0×10^3
$\dot{r}$	0.01	0.001
τ_c	{110} <111> : 500	{110} <111> : 260
	{112} <111> : 500	{112} <111> : 260
τ_0	{110} <111> : 260	{110} <111> : 140
	{112} <111> : 260	{112} <111> : 140
h_0	28,000	1200
a	3.25	2.0
m	20	20

be determined that when the material constitutive parameters were set values as shown in Table 5, and the simulation results can be well matched with the calculated results (Fig. 8).

3.5 Stress/strain distribution during deformation

Figure 9 shows the stress/strain distribution behavior of PF + B dual-phase model with different bainite contents at tensile strains of 5% and 25% conditions. As the tensile strain increased, a significant stress/strain gradient appeared in the model. In the initial stage of deformation, the strain was mainly distributed in polygonal ferrite, and as the strain continued to increase, there would also be a certain strain distribution in bainite. During the tensile deformation process, obvious strain concentration characteristics appeared. The strain concentration at B/PF interface was defined as C_{int}, and the strain concentration in polygonal ferrite was defined as C_P.

When the strain increased to 25%, both C_{int} and C_p points were observed (Fig. 9c–h, o–p). The content of bainite has a significant impact on the strain concentration characteristics. When the volume fraction of bainite was 18%, its strain concentration was mainly located in the polygonal ferrite, and a small amount of C_{int} points were observed (Fig. 9e, f). When the volume fraction of bainite increased to 35% (Fig. 9g, h), the strain concentration points at the phase interface significantly increased. When bainite reached 53% (Fig. 9o, p), only a few strain

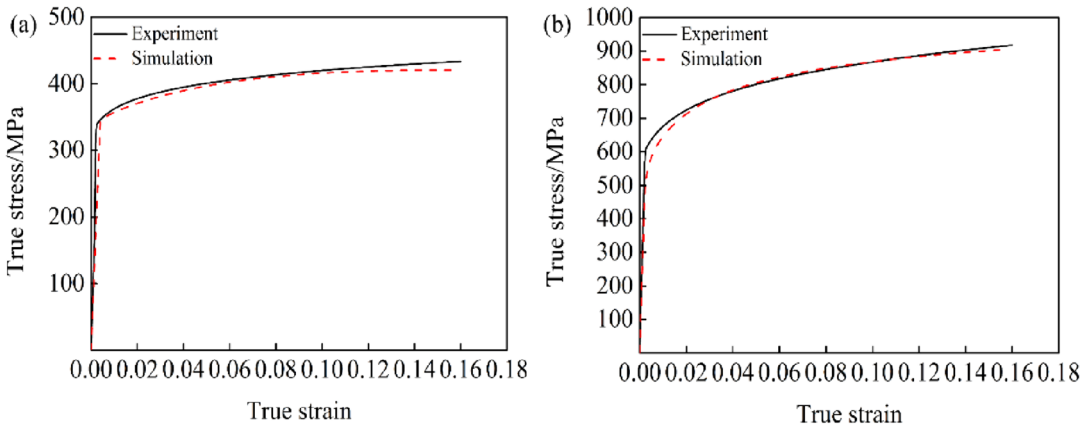

Fig. 8 Experiment and simulation stress–strain curves of polygonal ferrite (**a**) and bainite single phase (**b**)

concentration points in polygonal ferrite can be observed, while more linear strain concentration features appeared near the phase interface. As the volume fraction of bainite increased, the strain concentration in polygonal ferrite decreased, while the strain concentration at the phase interface increased. This indicated that the phase content was an important factor affecting the form of strain concentration behavior [29, 30].

Figure 10 shows the strain distribution rule in bainite and polygonal ferrite during tensile deformation. The variations of average strain and interphase strain difference during tensile deformation are shown in Fig. 11. As the tensile strain increased, the strain distribution of polygonal ferrite and bainite showed a normal distribution curve that shifted to the right as a whole, indicating that the strain distribution in two phases gradually increased. The average strain curves showed a linear increase pattern, and the average strain of polygonal ferrite was higher than that of bainite. However, there was a certain strain distribution in both phases, indicating a coordinated deformation behavior during tensile test. As the bainite content increased, the average strain in the bainite and polygonal ferrite phases gradually increased. During the tensile deformation, when the volume fraction of bainite was below 35%, increasing the content of bainite did not affect the strain difference between two phases. However, when the content of bainite reached 53%, the strain difference increased significantly.

The distribution and variation of stress are different. Figure 12 shows the stress distribution rule in polygonal ferrite and bainite during tensile deformation. Figure 13 shows the variations of average stress and interphase stress difference under different tensile strains. According to Figs. 9, 12, and 13, there was a significant stress gradient in polygonal ferrite and bainite, and the stress distribution in bainite was much higher than that in polygonal ferrite. As the tensile strain increased, the stress in polygonal ferrite gradually increased, but the maximum stress was still located in bainite. As the tensile strain increased, in addition to the bainite bearing stress, the polygonal ferrite also burdened a certain amount of stress due to strain hardening. Under the same strain conditions, as the bainite increased, the stress in bainite increased, and the peak stress distribution also increased. The stress difference between phases gradually increased with the increase in bainite content, but when the bainite content reached 53% and the tensile strain reached 25%, the increased amplitude was significantly increased.

The average strain of bainite and polygonal ferrite increased simultaneously, which contributed to the decrease of the strain difference among phases. In this case, the stress of both phases gradually increased under different tensile strains, indicating that a coordinated deformation behavior and strong strain hardening existed simultaneously. Therefore, when polygonal ferrite was the matrix (bainite content $< 50\%$) in PF + B dual phase steel, moderately increasing the bainite content will enhance the coordinated deformability, and this excellently coordinated deformability increased the average stress/strain of both phases simultaneously, thereby maximizing the plasticity of the material, which was beneficial to improving the strength and plasticity of the material.

However, when the bainite content reached 53%, the average strain in polygonal ferrite further increased. In contrast, the average strain increment in bainite significantly decreased, which induced uneven deformation of bainite and polygonal ferrite. Meanwhile, the average stress increase in polygonal ferrite was minimal, while the average stress increase in bainite was significant, further exacerbating the strength difference between the two phases. Strain and stress were distributed separately in polygonal ferrite and bainite, reducing the coordinated deformation ability of two phases, and easily causing interphase plastic damage.

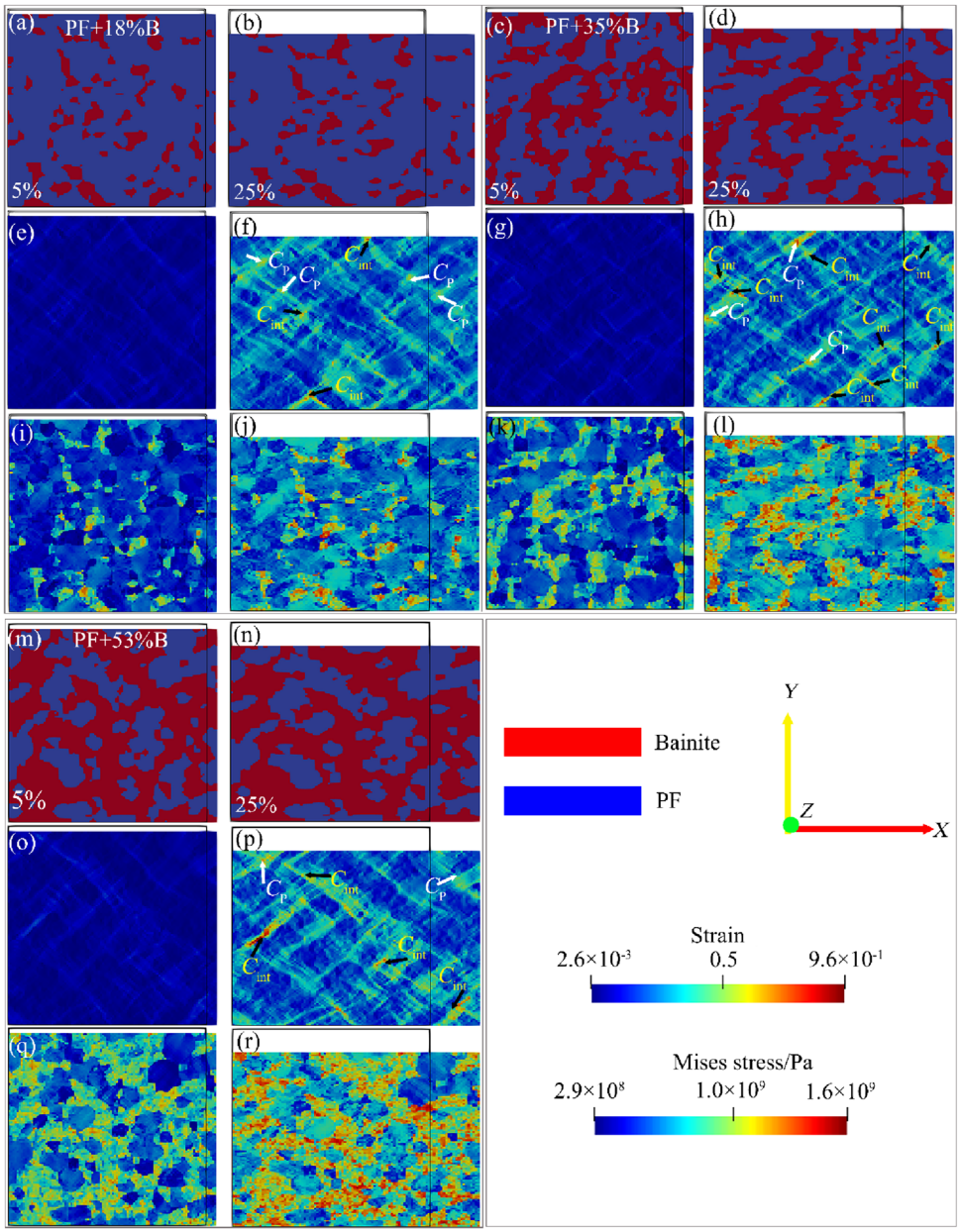

Fig. 9 Stress/strain distribution behavior of PF + B dual-phase model with different bainite contents at tensile strains of 5% and 25% of PF + 18%B model (**a**, **b**, **e**, **f**, **i**, **j**), PF + 35%B model (**c**, **d**, **g**, **h**, **l**) and PF + 53%B model (**m**–**r**). **a**–**d**, **m**, **n** Phase distribution maps; **e**–**h**, **o**, **p** strain distribution maps

4 Conclusions

1. When the volume fraction of bainite was 35%, PF + B dual phase steel showed the optimal strain hardenability and strength plasticity matching.
2. The 3D-CPFE analysis results indicated that with the increase in bainite content from 18% to 35%, the interphase coordinated strain hardening did not continuously increase the strain difference, and the stress distribution in polygonal and bainite phases increased simultaneously, improving the coordinated deformability, which was beneficial to improving the strength and plasticity.

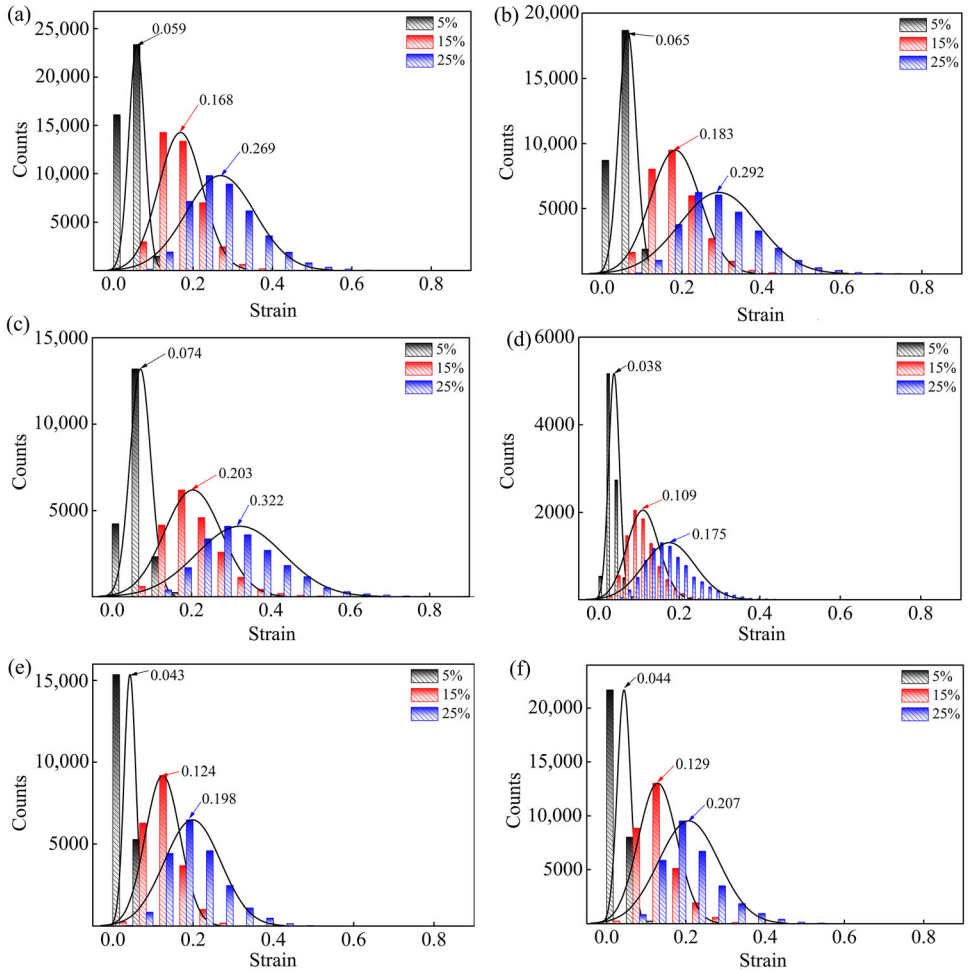

Fig. 10 Strain distribution behavior in polygonal ferrite (**a**–**c**) and bainite (**d**–**f**). **a**, **d** PF + 18%B model; **b**, **e** PF + 35%B model; **c**, **f** PF + 53%B model

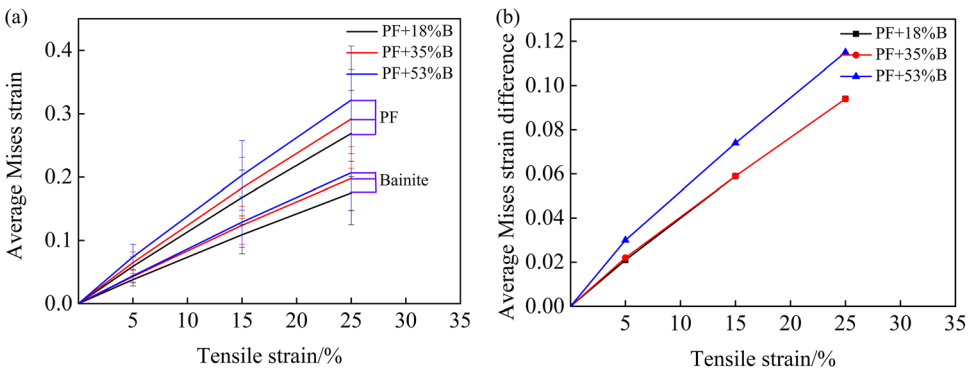

Fig. 11 Variations of average strain (**a**) and interphase strain difference (**b**) under different tensile strains

3. When the bainite content reached 53%, the deformability of ferrite was limited, exacerbating the non-uniformity of deformation between phases, increasing the interphase strain/stress difference, reducing the coordinated deformability between polygonal ferrite and bainite, and easily causing interphase plastic damage.

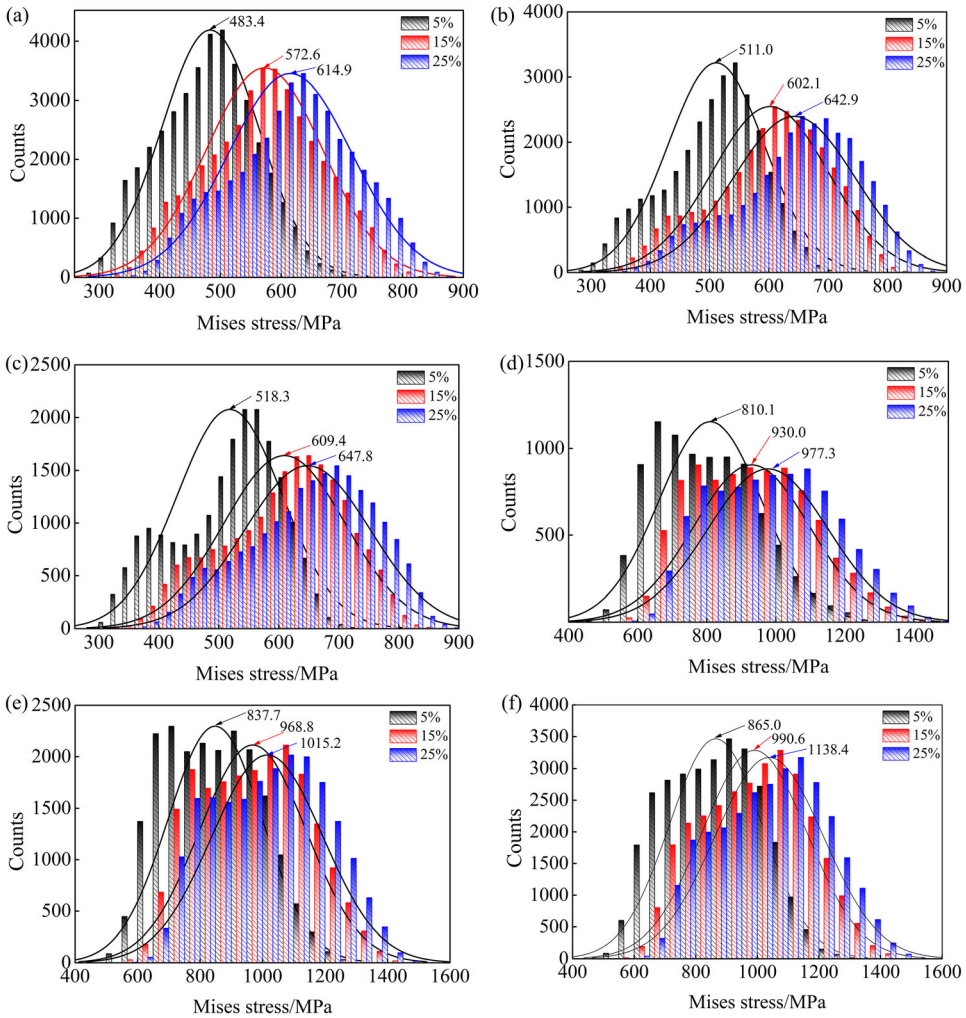

Fig. 12 Mises stress distribution behavior in polygonal ferrite (**a**–**c**) and bainite (**d**–**f**). **a**, **d** PF + 18%B model; **b**, **e** PF + 35%B model; **c**, **f** PF + 53%B model

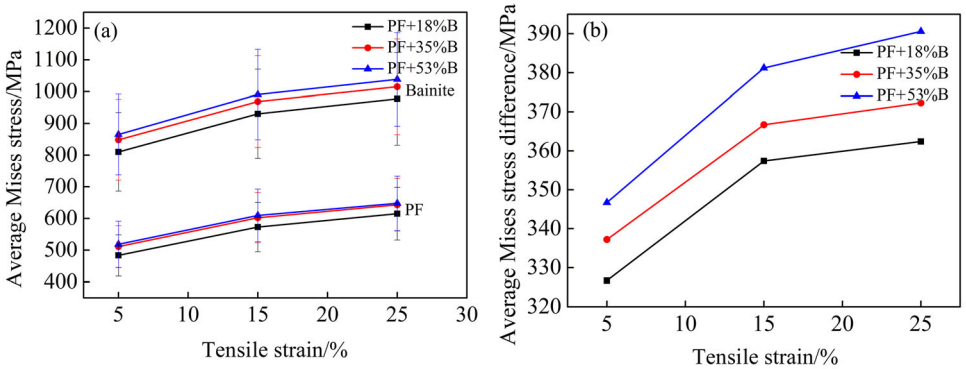

Fig. 13 Variations of average Mises stress (**a**) and interphase stress difference (**b**) under different tensile strains

Acknowledgements This work was supported by the Project of Liaoning Marine Economic Development (Development of high strength pipeline steel for submarine oil and gas transmission) and State Key Laboratory of Metal Material for Marine Equipment and Application Funding (No. SKLMEA-K202205).

Declarations

Conflict of interest Xian-bo Shi and Wei Yan are youth editorial board members for *Journal of Iron and Steel Research International* and were not involved in the editorial review or the decision to publish this article. The authors declare that they have no known competing financial interests or personal relationships that could have appeared to influence the work reported in this paper.

References

[1] X.B. Shi, W. Yan, W. Wang, L.Y. Zhao, Y.Y. Shan, K. Yang, J. Iron Steel Res. Int. 22 (2015) 937–942.
[2] A. Shukla, H. Karki, Robot. Auton. Syst. 75 (2016) 508–524.
[3] T. Xu, S. Guo, G. He, H. Han, J. Iron Steel Res. Int. 31 (2024) 488–500.
[4] Z.W. Tan, Z.B. Wang, S.Y. Bai, D.L. Zhang, S.Z. Zhang, F. Cheng, S.H. Xing, Y.H. Jin, J. Iron Steel Res. Int. 29 (2022) 1026–1038.
[5] A. Hilberink, A. Gresnigt, L. Sluys, in: Proceedings of the ASME 2011 30th International Conference on Ocean, Offshore and Arctic Engineering, Volume 4: Pipeline and Riser Technology, ASME, Rotterdam, The Netherlands. 2011. pp. 401–412.
[6] L. Muravyeva, N. Vatin, Appl. Mech. Mater. 633–634 (2014) 958–964.
[7] N. Ishikawa, M. Okatsu, S. Endo, J. Kondo, in: Proceedings of the 2006 International Pipeline Conference, Volume 3: Materials and Joining; Pipeline Automation and Measurement; Risk and Reliability, Parts A and B, ASME, Calgary, Alberta, Canada, 2006. pp. 215–222.
[8] X. Tu, X. Shi, Y. Shan, W. Yan, Q. Shi, Y. Li, C. Li, K. Yang, Mater. Sci. Eng. A 793 (2020) 139889.
[9] Y. Ren, X.B. Shi, Z.G. Yang, Y.Y. Shan, W. Ye, G.X. Cai, K. Yang, J. Iron Steel Res. Int. 28 (2021) 752–761.
[10] X. Tu, Y. Ren, X. Shi, W. Yan, Q. Shi, Y. Shan, C. Li, Mater. Today Commun. 33 (2022) 104923.
[11] X. Tu, Y. Ren, X. Shi, C. Li, W. Yan, Y. Shan, K. Yang, Materials 14 (2021) 5358.
[12] G.Y. Qiao, Z.T. Zhao, X.B. Shi, Y.Y. Shan, Y. Gu, F.R. Xiao, Materials 14 (2021) 5352.
[13] M.R. Akbarpour, A. Ekrami, Mater. Sci. Eng. A 477 (2008) 306–310.
[14] X. Zhang, H. Gao, X. Zhang, Y. Yang, Mater. Sci. Eng. A 531 (2012) 84–90.
[15] C.J. Tang, C.J. Shang, S.L. Liu, H.L. Guan, R.D.K. Misra, Y.B. Chen, Mater. Sci. Eng. A 731 (2018) 173–183.
[16] N. Ishikawa, K. Yasuda, H. Sueyoshi, S. Endo, H. Ikeda, T. Morikawa, K. Higashida, Acta Mater. 97 (2015) 257–268.
[17] W. Liu, J. Lian, N. Aravas, S. Münstermann, Int. J. Plast. 126 (2020) 102614.
[18] R.J. Asaro, J.R. Rice, J. Mech. Phys. Solids 25 (1977) 309–338.
[19] S.R. Kalidindi, J. Mech. Phys. Solids 46 (1998) 267–290.
[20] E.J. Shin, A. Jung, S.H. Choi, A.D. Rollett, S.S. Park, Mater. Sci. Eng. A 538 (2012) 190–201.
[21] J. Zhang, H. Ding, J.W. Zhao, Mater. Sci. Forum 816 (2015) 729–735.
[22] Q. Lai, O. Bouaziz, M. Gouné, L. Brassart, M. Verdier, G. Parry, A. Perlade, Y. Bréchet, T. Pardoen, Mater. Sci. Eng. A 646 (2015) 322–331.
[23] L. Cheng, W. Yu, Q.W. Cai, Q. Yang, Mater. Sci. Eng. A 812 (2021) 141122.
[24] P. Han, Z. Liu, Z. Xie, H. Wang, Y. Jin, X. Wang, C. Shang, Int. J. Miner. Metall. Mater. 30 (2023) 1329–1337.
[25] M.A. Groeber, M.A. Jackson, Integr. Mater. Manuf. Innov. 3 (2014) 56–72.
[26] W.C. Oliver, G.M. Pharr, J. Mater. Res. 7 (1992) 1564–1583.
[27] Y.W. Bao, W. Wang, Y.C. Zhou, Acta Mater. 52 (2004) 5397–5404.
[28] M. Dao, N. Chollacoop, K.J. Van Vliet, T.A. Venkatesh, S. Suresh, Acta Mater. 49 (2001) 3899–3918.
[29] Y. Hou, S. Cai, T. Sapanathan, A. Dumon, M. Rachik, Comput. Mater. Sci. 158 (2019) 243–254.
[30] J. Hu, X. Li, Q. Meng, L. Wang, Y. Li, W. Xu, Mater. Sci. Eng. A 855 (2022) 143904.